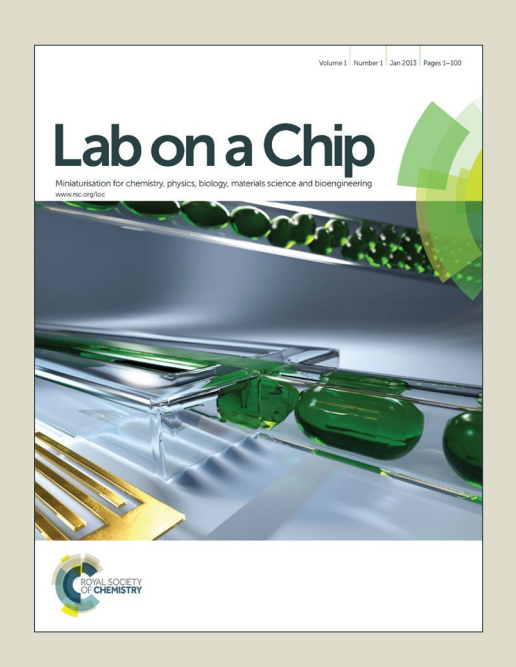
Lab on a Chip

Accepted Manuscript



This is an *Accepted Manuscript*, which has been through the Royal Society of Chemistry peer review process and has been accepted for publication.

Accepted Manuscripts are published online shortly after acceptance, before technical editing, formatting and proof reading. Using this free service, authors can make their results available to the community, in citable form, before we publish the edited article. We will replace this Accepted Manuscript with the edited and formatted Advance Article as soon as it is available.

You can find more information about *Accepted Manuscripts* in the **Information for Authors**.

Please note that technical editing may introduce minor changes to the text and/or graphics, which may alter content. The journal's standard <u>Terms & Conditions</u> and the <u>Ethical guidelines</u> still apply. In no event shall the Royal Society of Chemistry be held responsible for any errors or omissions in this *Accepted Manuscript* or any consequences arising from the use of any information it contains.



ROYAL SOCIETY OF CHEMISTRY

Lab on a Chip

ARTICLE

Received 00th January 20xx, Accepted 00th January 20xx

DOI: 10.1039/x0xx00000x

www.rsc.org/

Optofluidic restricted imaging, spectroscopy and counting of nanoparticles by evanescent wave using immiscible liquids

L. Liang, Y. F. Zuo, W. Wu, X. Q. Zhu and Y. Yang*

Conventional flow cytometry (FC) suffers the diffraction limit for the detection of nanoparticles less than 100 nm whereas traditional total internal reflection (TIR) microscopy can only detect the very few samples near the solid-liquid interface mostly in static states. Here we demonstrate a novel on-chip optofluidic technique using the evanescent wave sensing for single nanoparticle real time detection by combining the hydrodynamic focusing and the TIR using immiscible flows. The immiscibility of the high-index sheath flow and the low-index core flow naturally generates a smooth, flat and step-index interface that is ideal for the TIR effect, whose evanescent field can penetrate the full width of the core flow. The hydrodynamic focusing can focus all nanoparticles in the extreme centre of the core flow with the width less than 1 µm. This technique enables to illuminate every single sample in the running core flow by the evanescent field, leaving none evasive. Moreover, it works well for the samples much smaller than the diffraction limit. We have successfully demonstrated the scattering imaging and counting of 50-nm and 100-nm Au nanoparticles and also the fluorescent imaging and counting of 200-nm beads. The effective counting speeds are estimated 1500, 2300 and 2000 particles per second for the three types of nanoparticles, respectively. The optical scattering spectra are also been measured to determine the size of individual Au nanoparticle. This provides a new technique to detect nanoparticles and foresee the application in the detection of molecules for biomedical analyses.

Introduction

Detection of single molecules/nanoparticles using optical methods has great potential for the applications of biological and chemical sciences. [1-3] Flow cytometry (FC) has been used as a fundamental analytical tool for micro-scale samples detection, [4-7] providing a convenient and high-efficiency way to study the properties of cells and microorganisms. However, traditional FCs mostly illuminates the samples from far field and collects the scattered or fluorescent light [5-8]. Only averaged characteristics can be measured for a large collection of nanoparticles. It is an urge for today's research to measure the individual behaviour of single nanoparticles, which is still a big challenge to the traditional FCs. For example, the diffraction limit makes it very difficult to detect the nanoparticles below 100 nm.

Total internal reflection (TIR) microscopies are based on the principle of the evanescent wave sensing, which is usually created by the TIR between glass and water. ^[9, 10] The TIR generates an evanescent field that decays exponentially, generating an optical illumination system beyond the diffraction limit at the interface of two media. ^[11] The TIR microscopy has higher sensitivity and signal-

School of Physics & technology, Wuhan University, Wuhan 430072, China. E-mail: yangyiys@whu.edu.cn

to-noise ratio than the conventional ones. Therefore, it is one of the most widely used technologies in the detection of single nanoparticles/molecules. However, it still needs further improvement to satisfy the needs of today's research. For instance, the penetration depth into the sample medium is limited, and thus only the samples at the vicinity of the solid-liquid interface can be detected [12, 13]. In addition, detection systems with real-time control and rapid response should be applies to detect samples of interest. [5, 14, 15] Moreover, the increasing demand of point-of-care diagnosis makes it imperative to develop miniaturized systems.

Optofluidics draws on the strengths of both microfluidics and optics, and has inspired the creation of a variety of innovative onchip devices, such as optofluidic tunable mircrolenses[16-19], biosensors^[20-22], liquid-liquid waveguides^[23,24] and symmetric mirror channel structures^[25]. In this paper, we attempt to use immiscible liquids to build up a smooth and flat interface for a TIR device and demonstrate its function for real time nanoparticle sensing. A pure liquid system is found advantageous over the solid-liquid hybrid in several aspects. [26-29] For instance, hydrodynamic focusing [30, 31] using three flows (a core flow in the middle of two sheath flows) is able to narrow the core flow down to 50 nm and can be adjusted in real time to match the range of evanescent field by simply controlling the flow velocities. [30] Besides, the liquid-liquid interface between the core flow and the sheath flow is optical smooth. These two factors are beneficial to optofluidic devices. However, because the fast diffusion [32, 33] between miscible liquids smears the liquidARTICLE Lab Chip

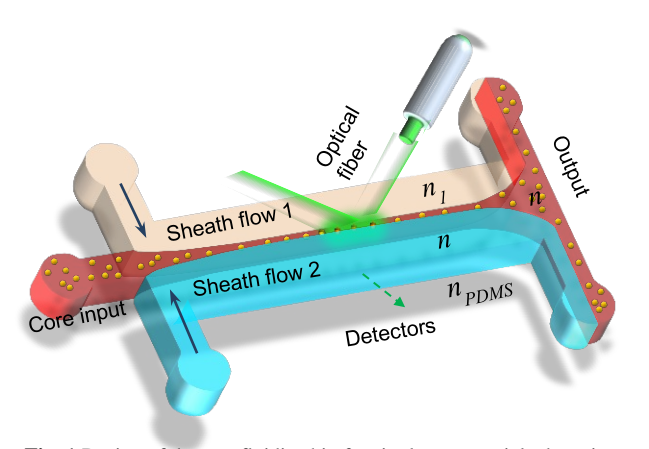


Fig. 1 Design of the optofluidic chip for single nanoparticle detection. All particles are conveyed in the very narrow core flow and can be detected by the evanescent field formed by the total internal reflection at the liquid/liquid interface of immiscible flows.

liquid interface and adversely affects the detection, immiscible liquids system is more advantageous. [34] Usually immiscible liquids are used to generate liquid droplets. [35, 36] Here, we creatively use oil with low viscosity and ethylene glycol solution, which are incompatible with each other. It can provide good physical conditions for TIR by adjusting the liquid refractive index of oil and the ethylene glycol solution, and ensured that the ideal TIR interface without bending by matching the viscosity coefficients. All nanoparticles are conveyed in the core flow, whose width is adjusted to be smaller than penetration depth of evanescent field. Therefore, all nanoparticles in the core flow of this optofluidic device can be detected, even for nanoparticles whose size is smaller than the diffraction limit. To strengthen the detection functionality based on the existing experimental and scattering law, [37, 38] the scattering

imaging of 50-nm and 100-nm Au nanoparticles and the fluorescent imaging of 200-nm fluorescent beads are demonstrated, while the optical scattering spectra of individual flowing nanoparticles are measured as well. The scattering or fluorescent signals excited by the evanescent wave also been used for nanoparticle counting.

Working principle and conceptual design

Device design

Figure 1 shows the schematic of the immiscible liquid-liquid optofluidic device based on the TIR for nanoparticle detection. The sheath flow 1 is immiscible with the core flow, and its refractive index n_1 is slightly higher than that of the core flow n while their viscosity ratio is close to 1 to obtain a flat interface in the vertical direction for the TIR effect. By adjusting the flow rates and the flow rate ratio, the core flow can be squeezed to make the samples suspended in the core flow move one by one, like a string of pearls. As compared to the miscible liquid-liquid interface, the immiscible liquids causes no diffusion across the interface and thus forms a step changes of refractive indices, resulting in a stable evanescent field. Besides, the whole microchannel structure is made polydimethylsiloxane (PDMS), and n_1 is intentionally chosen to match the refractive index n_{PDMS} of PDMS. As a result, the interface of PDMS and the sheath 1 does not affect the light propagation. The input light comes from an optical fiber that is buried in the PDMS layer. The light is collimated by an on-chip lens [24] to ensure the incident ray to be parallel at the interface of the sheath flow 1 and the core flow. When the incident angle is larger than the critical angle, the incident ray experiences the TIR and generates the evanescent wave along the width direction of the core flow. When

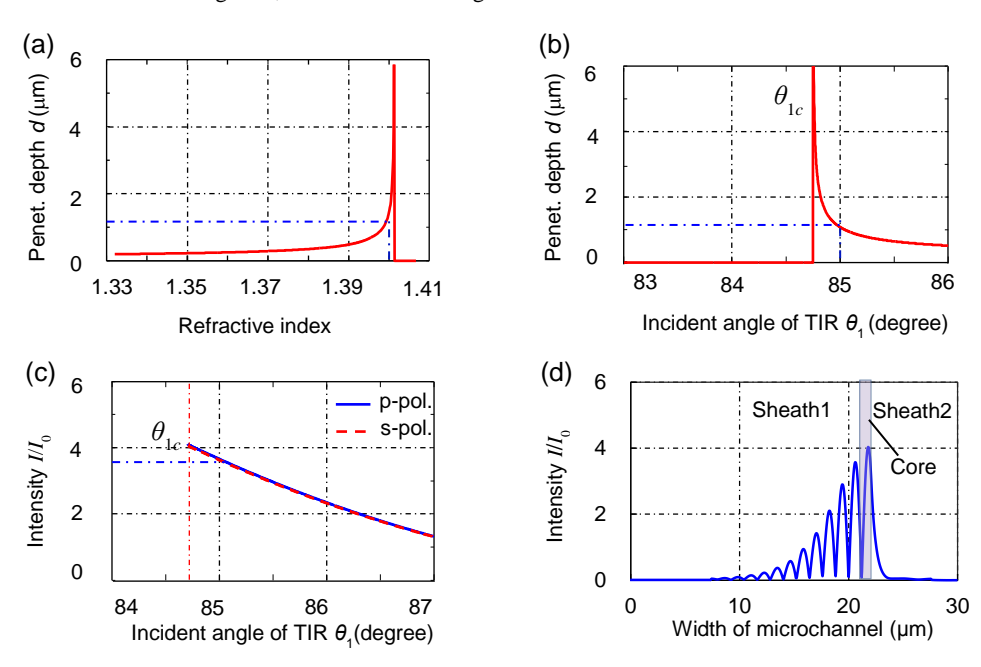


Fig. 2 Analytical relationships of the evanescent field of total internal reflection. (a) and (b) Penetration depth d as functions of refractive index n of the core flow and the incident angle θ , respectively. For n = 1.40 and $\theta = 85^{\circ}$, it has $d \approx 1$ µm. (c) Normalized intensities I/I_0 of the evanescent field for both the s-polarized and p-polarized lights, where I is the field intensity and I_0 is the intensity of incident light. (d) Intensity distribution along the width direction of the microchannel.

Lab Chip ARTICLE

the width of core flow is narrower than the penetration depth of the evanescent field, all the samples conveyed in the core flow can be illuminated by the evanescent wave. Besides, two light sources, a 532-nm laser and a supercontinuum white source, have been used for the detection and spectroscopy, respectively. [37, 38]

Analytical relationships

The reflection in the liquid-liquid interface follows the Snell's law $n \sin \theta = n_1 \sin \theta_1$ (1)

where θ_1 and θ are the angles of the incident rays and the refractive light, respectively. In this work, there are $n_1 = 1.406$ and n = 1.400. In the critical state the refracted angle is $\theta = 90$ °, correspondingly the critical incident angle is $\theta_{Ic} = 84.7$ °.

In the TIR state, the electromagnetic radiation penetrates into the low refractive index medium (here is the core flow) and generates the evanescent field. The penetration depth is defined as the depth at which the intensity of the radiation falls to 1/e of that at the interface. The penetration depth d is related to the incident angle θ_1 by $^{[39]}$

$$d = \frac{\lambda_0}{4\pi n_1} \left[\sin^2 \theta_1 - (n/n_1)^2 \right]^{-1/2}$$
 (2)

where λ_0 is the incident wavelength. For $\lambda_0 = 532$ nm, $\theta_1 = 85^\circ$ and $n_1 = 1.406$, the relationship of d and n is plotted in Fig. 2(a). It shows that the closer the value of n is to n_1 , the deeper the penetration depth can be. For $n_1 = 1.406$ and n = 1.400, the relationship between d and θ_1 is plotted in Fig. 2(b). The penetration depth goes to nearly 6 μ m when the incident angle is close to θ_{1c} , and drops gradually with the further increase of θ_1 . In this case of $\theta_1 = 85^\circ$, it has $d \approx 1$ μ m.

The intensities of the evanescent field for both the s-polarized light and the p-polarized light as a function of the incident angle can be expressed as ^[39]

$$I(P) = I_0(P) \frac{4\cos^2\theta_1(2\sin^2\theta_1 - (n/n_1)^2)}{(n/n_1)^4\cos^2\theta_1 + \sin^2\theta_1 - (n/n_1)^2}$$
(3)

$$I(S) = I_0(S) \frac{4\cos^2 \theta_1}{1 - (n/n_1)^2} \tag{4}$$

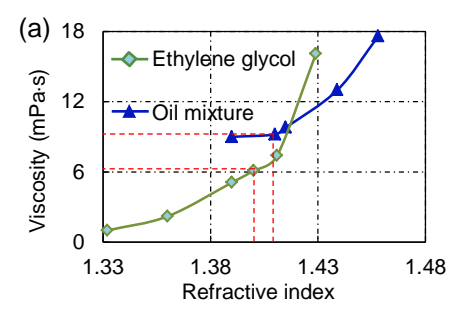
For n=1.400 and $n_1=1.406$, the refractive index contrast is 0.006. In this case, the intensities of evanescent fields of both the s-light and p-polarized light are plotted in Fig. 2(c). It is seen that the two curves almost fully overlap with each other, or equivalently, the intensity of evanescent field is polarization independent. This feature saves the need for precise polarization control and is beneficial to the TIR. When the incident angle θ_1 is below the critical angle θ_{1c} , the intensities are zero. At $\theta_1 = \theta_{1c}$, the relative intensity goes down gradually. In the special case of $\theta_1 = 85^\circ$, it has $I/I_0 \approx 3.5$. Fig. 2(d) shows the intensity of the evanescent field along the width direction of the microchannel. In the sheath flow 1, an interference pattern is observable. In the core flow, the decay of the evanescent field is presented. It can be seen that the width of the core flow is totally covered by the evanescent wave for detections.

Experimental results and discussions

Fabrication

In this experiment, the microchannel structrure was fabricated by the standard soft photolithographic processes. First, a layer of SU-8 photoresist (Micro–Chem, SU-8) was spin-coated onto a silicon substrate. After pre-baking, the SU-8 film was exposed to UV light under a glass mask using a mask aligner (OAI, 506). Then, a positive relief of photoresist on the surface was generated, which would be used as the mold for later replication. Then, PDMS (Momentive RTV615) was poured over the mold and baked in an oven at 75 °for 1 h. The PDMS replica was then peeled off and sealed against a flat PDMS slab to form the microchannel after oxygen plasma bonding. After the fabrication, the microchannel has the width $W = 30 \mu m$ and the height $H = 20 \mu m$.

The flows are pumped into the microchannel from the central and the outer inlets using syringe pumps. For experiments, the materials of three flows are, respectively, the ethylene glycol solution as the core flow and sheath flow 2, and the oil mixture as the sheath flow 1. Because the oil mixture and the ethylene glycol solution are immiscible, their interface can be smooth without diffusion. A thinned optical fiber [40] is integrated to let the 532-nm laser or the supercontinuum white source as the source for detection and spectroscopy. An air lens, which is the plano-concave, the radius of curvature R = 70 μ m and the thickness D = 60 μ m, is employed to collimate the incident light in PDMS. [24] The incident angle is θ_1 = 85 °, the same as that for the analysis in Fig. 2.



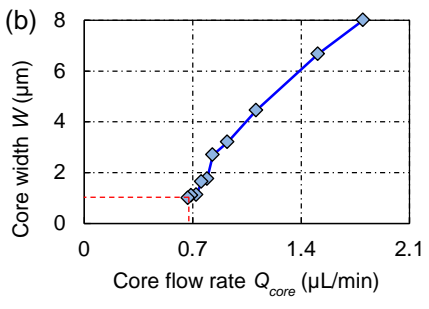


Fig. 3 Measured properties of the liquid materials in the microchannel. (a) The viscosity μ with respect to the refractive index for the ethylene glycol aqueous solution and the oil mixture. (b) The core width as a function of the flow rate of the core flow. Here the sheath 1 uses the oil mixture (92.5% silicone oil and 7.5% paraffin oil) with n_{sheath} 1 = 1.406 and μ_{sheath} 1 = 9.2 mPa·s; the core flow and the sheath 2 uses the same material of ethylene glycol aqueous solution (30% DI water and 70% ethylene glycol) with n_{core} = n_{sheath} 2 = 1.40, μ_{core} = μ_{sheath} 2 = 6.0mPa·s. At Q_{sheath} = 9.0 μL/min and Q_{sheath} = 3.5 μL/min, the core flow narrows down with the decrease of the rate of core flow Q_{core}. At Q_{core} = 0.55μL/min, the width of core flow is down to about 1 μm.

ARTICLE Lab Chip

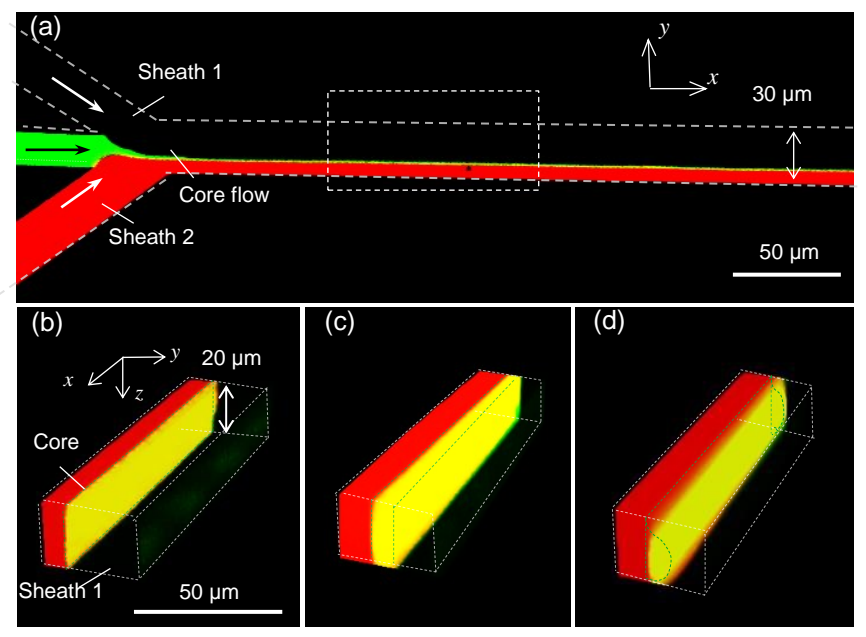


Fig. 4 Measured configuration of the flows in the microchannel, which is 30 μm wide and 20 μm high. (a) Top view of the hydrodynamically focused flows at $Q_{core} = 0.55$ μL/min. For the sheath flows, the flow rates are always kept at $Q_{sheath1} = 9.0$ μL/min and $Q_{sheath2} = 3.5$ μL/min. (b) the 3D fluidic structure of the dashed square region in (a) measured by the confocal microscopy, the width of core flow is about 1 μm. (c) and (d) have the same flow rate $Q_{core} = 1.8$ μL/min and the similar width of core flow of about 8 μm, but they have different viscosities of the sheath flow 1. The interface between the sheath flow 1 and the core flow is straight in the vertical direction in (c), but curved in (d). The viscosity of the sheath flow 1 is 9.2 mPa·s in (c) but 24.4 mPa·s in (d), the former is close to that of the core flow 6.0 mPa·s.

Measured flow configuration

In order to get a smooth, flat and step-index interface for the TIR, the viscosities and the refractive indices of the liquids, respectively measured by viscometer (Yutong Instrument, NDJ-8s) and refractometer (ATAGO, PAL-RI), should be chosen carefully. The relationships are plotted in Fig. 3(a) as measured in experiment. Both curves show the same trend that the viscosity increases with the refractive index. The ethylene glycol aqueous solution is prepared by using pure ethylene glycol and DI water. The refractive index n = 1.400 is obtained by mixing 30% DI water with 70% ethylene glycol in mass. Correspondingly, the viscosity is 6.0 mPa·s. The oil mixture is made of silicone oil and paraffin oil, the refractive index of the oil mixture increases with the proportion of paraffin oil. When the refractive index is $n_1 = 1.406$ (92.5% silicone oil and 7.5% paraffin oil in mass), the viscosity is 9.2 mPa·s.

As the width of the core flow is essential for the evanescent wave sensing, its relationship with the rate of core flow is measured as shown in Fig. 3(b). It is seen that a lower core flow rate leads to a narrower core. For instance, when $Q_{sheath1}=9.0~\mu\text{L/min}$ and $Q_{sheath2}=3.5~\mu\text{L/min}$, the core flow narrows down with the decrease of the rate of core flow Q_{core} . At a special case of $Q_{core}=0.55~\mu\text{L/min}$, the width of core flow is down to about 1 μ m, roughly matching the penetration depth of evanescent field. The core width can be further reduced by slowing down the core flow rate. In this measurement, the core flow is pumped at 0.5 μ L/min as much as possible.

To visualize the interface between the core flow and sheath flow 1 after the hydrodynamic focusing, the laser scanning confocal

microscopy (Nikon, A1R) is used to monitor the 3D liquid spatial profiles in the microchannel as shown in Figure 4. The core flow is dyed with Rhodamine 6G to emit yellow fluorescence when excited by an argon ion laser (wavelength 488 nm), and the sheath flow 2 is mixed with Rhodamine B to give red fluorescence by a DPSS laser (wavelength 561 nm), but the sheath flow 1 has no dye. The 3D fluidic structure of the microchannel are scanned using a Z-stacked mode at the 1-µm interval using an inverted optical microscope and a 10×/0.3 NA objective lens. Fig. 4(a) shows the top view of the hydrodynamically focused flows when the core flow rate is Q_{core} = $0.55\ \mu L/\text{min}.$ For the sheath flows, the flow rates are always kept at $Q_{sheath1} = 9.0 \mu L/min$ and $Q_{sheath2} = 3.5 \mu L/min$. Fig. 4(b) – (d) shows the 3D structures of the dashed-square region of Fig. 4(a). It is seen clearly from Fig. 4(b) that the interface between the core flow and the sheath flow 1 is straight in the vertical direction, which is critical to the optical confinement in the vertical direction for the TIR effect. In Fig. 4(c) and (d), they have the same flow rate $Q_{core} = 1.8 \mu L/min$ and thus the similar width of core flow of about 8 µm. The difference lies in the viscosity. In Fig. 4(c), the viscosity of the sheath flow 1 is 9.2 mPa·s, which is close to that of the core flow 6.0 mPa·s. As a result, the interface is approximately flat in the vertical direction. In contrast, in Fig. 4(d) the viscosity of the sheath flow 1 is 24.4 mPa·s (Pure paraffin oil without mixture), which is apparently larger than that of the core flow 6.0 mPa·s. Such a mismatch causes the interface to be curved in the vertical direction. This is unfavourable for the TIR effect.

Evanescent field and nanoparticle detection

Lab Chip ARTICLE

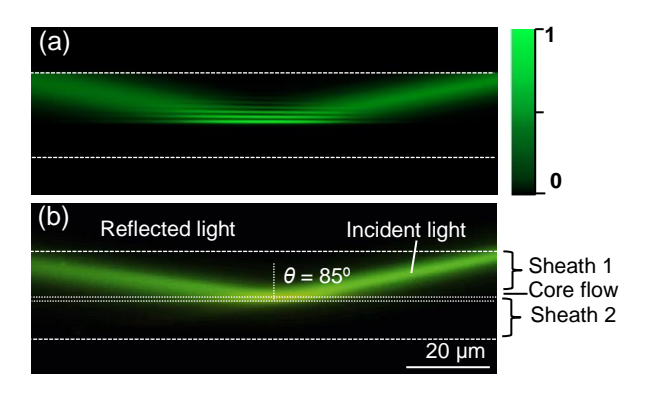


Fig. 5 Optical intensity distribution of the evanescent field generated by the total internal reflection at the liquid/liquid interface between the sheath flow 1 and the core flow. (a) Simulated result; (b) measured fluorescent micrograph.

The simulated optical field of the TIR at the liquid/liquid interface between the core flow and the sheath flow 1 is shown in Fig. 5(a), here the incident light has the wavelength of 532 nm. The measured fluorescent image (incident wavelength 532 nm, green laser (CNI MGL-FN-532/1, 500 mW)) is shown in Fig. 5(b). They agree with each other. In this experiment, the incident angle is set at 85 °, larger than the critical angle 84.7 °, the flow rates are $Q_{core}=0.55\,\mu\text{L/min}$, $Q_{sheath1}=9.0\,\mu\text{L/min}$ and $Q_{sheath2}=3.5\,\mu\text{L/min}$. For visualization, the core flow and the sheath flow 2 are both dyed with Rhodamine 6G, and the sheath flow 1 is added with Nile Red. It is seen clearly in Fig. 5(b) that the TIR evanescent field well covers the whole width of the core flow. Obviously, the intensity of evanescent filed is much stronger than that of the incident and reflected lights. As the evanescent wave is the light source, the strong intensity is beneficial

to the illumination of core flow. Therefore, the single nanoparticles conveyed in the core flow can be illuminated to scatter light and/or emit fluorescent light. This makes all of them detectable, leaving none evasive. For this reason, it is suitable for small particles, such as nanoparticles and even single molecules. And the concentration of the fluorescent polystyrene bead with the diameter of 200 nm is 24 \times 10⁶ particles /ml and the concentrations of the Au nanoparticles with the diameters of 50 nm and 100 nm are respectively 21×10^6 particles/ml and 41 $\times 10^6$ particles/ml. Fig. 6 shows the experimental proofs. In Fig. 6(a) and (b), the scattering images of the Au nanoparticles with the diameters of 50 nm and 100 nm are shown, respectively. The Au nanoparticles can be visualized clearly, thanks to the strong scattering. In Fig. 6(c), it shows the fluorescent image (not the scattering image) of the fluorescent polystyrene bead with the diameter of 200 nm. The image is also clear and sharp. These well prove that the evanescent field can light up the single nanoparticles in the core flow for optical detection spectrum.

Furthermore, the spectrum of each particle can be measured. Fig. 6(c) shows, from top to bottom, the scattering spectrum of the 50-nm Au nanoparticles, the scattering spectrum of the 100-nm Au nanoparticles, and the fluorescent spectrum of the 200-nm polystyrene bead. For simplicity, all the spectra are normalized, and spectra of the flowing nanoparticles each are collected 5 times to repeat. Here the incident light is a high-power supercontinuum white laser (Fianium, WhiteLase SC400), and the spectrum is taken by the spectrograph microscope system including the microscopy (Nikon, ECLIPSE Ti-U), EMCCD (Andor, iXon Ultra) and CCD (Andor, Newton 920) with Andor's line of Shamrock imaging spectrographs (Andor, Shamrock 303i). According to the scattering spectra of the 50-nm and the 100-nm Au nanoparticles, each has a scattering peak that corresponds to the plasmonic resonance of the Au nanoparticles

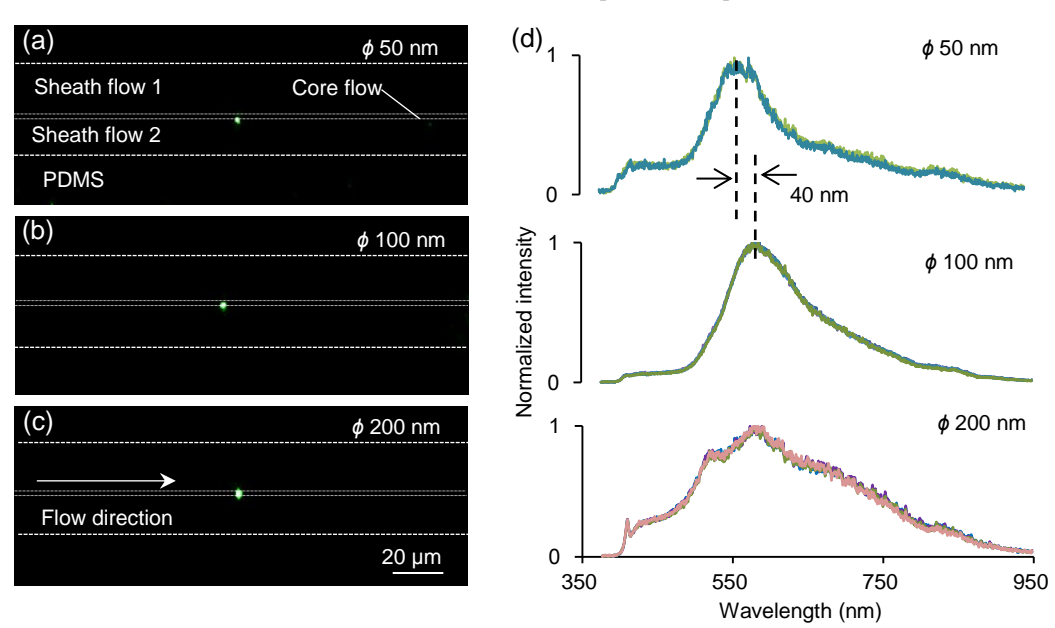


Fig. 6 Restricted images and spectra of the single particles in the core flow as illuminated by the evanescent field of total internal reflection. (a) Scattering image of a 50-nm Au nanoparticle; (b) scattering image of a 100-nm Au nanoparticle; and (c) fluorescent image of a 200-nm fluorescent bead. (d) Normalized spectra as illuminated by the supercontinuum white laser source, including (from top to bottom) the scattering spectrum of the 50-nm Au nanoparticle, the scattering spectrum of the 100-nm Au nanoparticle and the fluorescent emission spectrum of the 200-nm fluorescent bead. The spectra of the flowing nanoparticles each are collected 5 times in figure (d).

ARTICLE Lab Chip

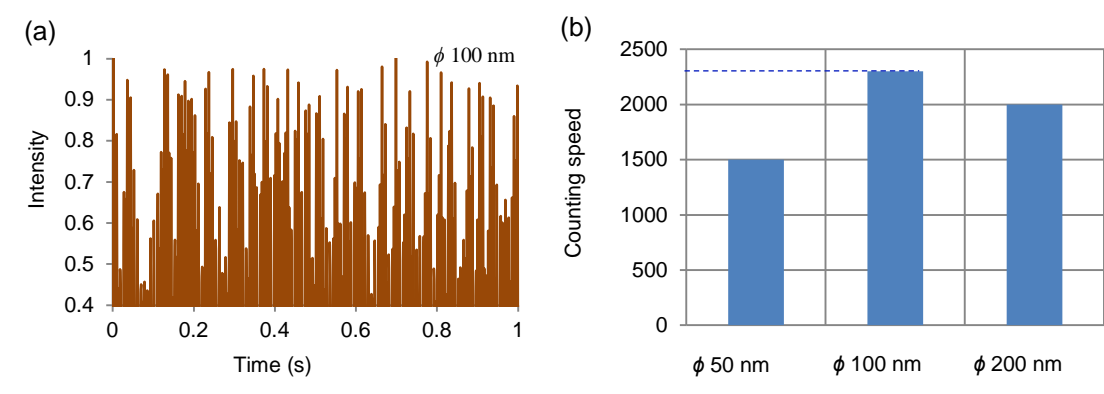


Fig. 7 Counting of nanoparticles when they flow through the detection point. (a) Intensity record of the light scattered by the 100-nm Au nanoparticles, the time range is 1 s. (b) Counts of the three types of nanoparticles as measured in 1 s. The types of nanoparticles are 50-nm Au nanoparticles, 100-nm Au nanoparticles and 200-nm fluorescent polystyrene beads.

[37] and the peak is shifted to longer wavelength with the increase of the nanoparticle size. This matches well with the existing experimental studies and the scattering law. [37, 38] For the 50-nm and 100-nm nanoparticles, the spectral shift is about 40 nm. Since the plasmonic resonant peak has a one-to-one relationship with the size of the Au nanoparticle, the spectroscopic study can be used to determine the size of Au nanoparticles from the plasmonic peak of the scattering spectrum. [37, 38] At the bottom of Fig. 6(d), the spectrum of fluorescent bead presents a wide linewidth, which differs from the scattering spectra of Au nanoparticles. Thus, the onchip TIR enables to detect and identity nanoparticles not only by the fluorescence but also by the scattering. The latter is particularly important for the nanoparticles smaller than the diffraction limit. The experimental studies of the 50-nm and 100-nm Au nanoparticles have well proven such a capability. Therefore, our optofluidic technique provides a convenient and highly-efficient method to study the nanoparticle size based on the restricted images and spectrum. After this technology is repeatedly verified, it can obtain the information of nanoparticles with several sizes in the fluid.

In addition, the scattering and/or fluorescent signals excited by the evanescent wave can be used for nanoparticle counting. The results are shown in Fig. 7. The 532-nm green laser (CNI MGL-FN-532/ 1,500mW) is used as source and the Hamamatsu's SCMOS camera is used for dynamic imaging of single particles. Its extraordinary signal-to-noise makes it superior to the conventional CCD cameras, even when it is operated at fast readout speed. The fastest readout speed at the central position reaches approximately 1,500 frames per second and the exposure time can be as short as 50 us, making the SCMOS camera ideal for dynamic acquisition of transient signals. Three types of nanoparticles are tested, i.e., 50-nm Au nanoparticles, 100-nm Au nanoparticles and 200-nm fluorescent polystyrene beads. As stated above, the Au nanoparticles are measured by the scattered light while the fluorescent polystyrene bead is by the fluorescence. Fig. 7(a) shows the signals of the recorded intensity of the 100-nm Au nanoparticles over 1 s. This enables to count the nanoparticles. When the flow rates are Q_{core} =0.55 μ L/min, $Q_{sheath1}$ = 9.0 μ L/min and $Q_{sheath2}$ = 3.5 μ L/min, the counting speed for the 100-nm Au nanoparticles reaches N = 170counts per second under the maximum readout speed of SCMOS with r = 0.074, here r is the ratio of the exposure time to the cycle time. Therefore, the effective counting speed is estimated $N_e = N / r$. For the 100-nm Au nanoparticles, it is $N_e = 2300$ particles per second. Further experiments under the same fluidic conditions yield that $N_e = 1500$ particles per second for the 50-nm Au nanoparticles and $N_e = 2000$ particles per second for the 200-nm fluorescent nanoparticles. The data are plotted in Fig. 7(b). These well demonstrate the capability of this optofluidic device for nanoparticle counting.

Conclusions

This paper presents an original work of real-time imaging, spectroscopy and counting of nanoparticles using the evanescent wave at the interface between immiscible liquids. By matching the viscosities and refractive indices of liquids, the interface can be flat and smooth, which is essential for the TIR effect. The key idea here is to narrow the core flow by the hydrodynamic focusing technique to have the width of about 1 µm, which can be fully covered by the evanescent field of TIR. It enables to detect all nanoparticles conveyed one by one in the running core flow, no matter how small the particles are. This is distinctively different from the conventional TIR fluorescent flow cytometers that can only detect the particles near the interface. Experiments have demonstrated the successful realizations of the real-time detection, spectroscopy and counting of different types of nanoparticles such as the 50-nm Au nanoparticles, the 100-nm Au nanoparticles and the 200-nm fluorescent beads. The effective counting speeds reach 1500, 2300 and 2000 particles per second for the three types of nanoparticles, respectively. This work provides a new technique to detect the nanoparticles and foresee the application in the detection of molecules for biomedical analyses.

Acknowledgement

This work was financially supported by grants from National Natural Science Foundation of China (No. 61378093), Hubei Provincial Natural Science Foundation (No. 2014CFA033), the Fundamental Research Funds for the Central Universities (No. 2042014kf0299).

Notes and references

- B. K. Patterson, M. Till, P. Otto, C. Goolsby, M. R. Furtado, L. J. McBride and S. M. Wolinsky, Science, 1993, 260, 976–979.
- 2 T. Pawson, Nature, 1995, **373**, 573–580.
- P. C. H. Li and D. J. Harrison, Anal. Chem., 1997, 69, 1564– 1568.

Lab Chip ARTICLE

- 4 H. M. Shapiro, *Practical Flow Cytometry*, John Wiley & Sons, 2005
- 5 X. Mao, Z. I. Stratton, A. A. Nawaz, S. C. S. Lin and T. J. Huang, Biomicrofluidics, 2010, 4, 043007.
- 6 A. Y. Fu, C. Spence, A. Scherer, F. H. Arnold and S. R. Quake, Nat. Biotechnol., 1999, 17, 1109–1111.
- 7 H. Tang and Y. F. Gao, IEEE Sens., 2005, **5**, 1346–1352.
- 8 S. H. Cho, J. M. Godin, C.H. Chen, W. Qiao, H. Lee and Y.H. Lo, Biomicrofluidics, 2010, 4, 043001.
- T. Funatsu, Y. Harada, M. Tokunaga, K. Saito and T. Yanagida, Nature, 1995, 374, 555–559.
- 10 M. Gu, J. B. Haumonte, Y. Micheau, J. W. Chon and X. Gan, Appl. Phys. Lett., 2004, 84, 4236–4238.
- 11 R. F. Marchington, M. Mazilu, S. Kuriakose, V. Garc és-Ch ávez, P. J. Reece, T. F. Krauss, M. Gu and K. Dholakia, Opt. Express, 2008, 16, 3712–3726.
- 12 J. Wang, B. Fei, R. L. Geahlen and C. Lu, Lab chip, 2010, 10, 2673–2679
- 13 J. Wang, N. Bao, L. L. Paris, R. L. Geahlen and C. Lu, Anal. Chem., 2008, 80, 9840–9844.
- 14 H. Zhang, C. H. Chon, X. Pan and D. Li, Microfluid. Nanofluid., 2009, 7, 739–749.
- 15 X. Wu, C. H. Chon, Y. N. Wang, Y. Kang and D. Li, Lap chip, 2008, 8, 1943–1949.
- 16 N. Hashemi, J. S. Erickson, J. P. Golden and F. S. Ligler, Biomicrofluidics, 2011, 5, 032009.
- 17 B. R. Watts, T. Kowpak, Z. Zhang, C.Q. Xu and S. Zhu, Biomed. Opt. Express, 2010, 1, 848–860.
- 18 B. R. Watts, Z. Zhang, C.Q. Xu, X. Cao and M. Lin, Biomed. Opt. Express, 2012, 3, 2784–2793.
- S. H. Cho, C. H. Chen and Y. H. Lo, Proc. of SPIE, 2011, 8099, 117–122.
- 20 J. Guo, X. Ma, N. V. Menon, C. M. Li, Y. Zhao and Y. Kang. IEEE J. Sel. Topics Quantum Electron., 2015, 21, 1-7.
- 21 N. T. Huang, S. C. Truxal, Y. C. Tung, A. Y. Hsiao, G. D. Luker, S. Takayama and K. Kurabayashi, Anal. Chem., 2010, 82, 9506–
- 22 H. Zhu, S. Mavandadi, A. F. Coskun, O. Yaglidere, and A. Ozcan, Anal. Chem., 2011, 83, 6641–6647.
- 23 P. Fei, Z. Chen, Y. Men, A. Li, Y. Shen and Y. Huang, Lab Chip, 2012, 12, 3700–3706.
- 24 Y. Shi, L. Liang, X. Q. Zhu, X. M. Zhang and Y. Yang, Lab Chip, 2015, 15, 4398-4403.
- 25 X. Wu, Y. Kang, Y. N. Wang, D. Xu and D. Li, Electrophoresis, 2008, 29, 2754–2759.
- 26 X. C. Li, J. Wu, A. Q. Liu, Z. G. Li, Y. C. Seow, H. J. Huang, K. Xu and J. T. Lin, Appl. Phys. Lett., 2008, 93, 193901.
- 27 D. Psaltis, S. R. Quake and C. Yang, Nature, 2006, 442, 381–386
- 28 Y. Yang, A. Q. Liu, L. Lei, L. K. Chin, C. D. Ohl, Q. J. Wang
- and H. S. Yoon, Lab Chip, 2011, **11**, 3182–3187.

 29 Y. Yang, L. K. Chin, J. M. Tsai, D. P. Tsai, N. Zheludev, and A.
- Q. Liu, Lab Chip,2012,12, 3785-3790.
- 30 J. B. knight, A. Vishwanath, J. P. Brody and R. H. Austin, Phys. Rev. Lett., 1998, **80**, 3863.
- 31 J. P. Golden, G. A. Justin, M. Nasir and F. S. Ligler, Anal. Chem., 2012, 402, 325–335.
- 32 Y. Yang, A. Q. Liu, L. K. Chin, X. M. Zhang, D. P. Tsai, C. L. Lin, C. Lu, G. P. Wang, and N. I. Zheludev, Nat. Comm., 2012, 3, 651.
- 33 Y. Yang, J. M. Tsai, D. L. Kwong and A. Q. Liu, IEEE 25th International Conference on Micro Electro Mechanical Systems, 2012, pp. 156–159.
- 34 C. Bernabini, D. Holmes and H. Morgan, Lab Chip, 2011, 11, 407-412.
- B. Zhang, J. D. Tice, and R. F. Ismagilov, Anal. Chem. 2004, 76, 4977-4982.

- 36 D. J. Collins, A. Neild, A. deMello, A. Q. Liu and Y. Ai, Lab Chip, 2015, 15, 3439-3459.
- 37 L.B. Scaffardi, N. Pellegri, O. De Sanctis, and J. O. Tocho, Nanotechnology, 2005, 16, 158.
- 38 C. Sönnichsen, S. Geier, N. E. Hecker, G. Von Plessen, J. Feldmann, H. Ditlbacher, B. Lamprecht, F. R Aussenegg, V. Z-H. Chan, J. P. Spatz and M. Möller, Appl. Phys. Lett., 2000, 77, 2949-2951.
- 39 D. Axelrod, T. P. Burghardt and N. L. Thompson, Ann. Rev. Biophys. Bioeng., 1984, 13, 247-268.
- 40 Y. Yuan, L. Wang, L. Ding and C. Wu, Appl. Opt., 2012, **51**, 5845-5849.